ARL-TR-10254 • JAN 2026

Environmental Impact on Directed Energy, Volume 1 (Directed Energy and Cloud Shadows)

by Gail Vaucher, Michael Lee, and Andrew Gatzke

NOTICES

Disclaimers

ARL-TR-10254 ● JAN 2026

Environmental Impact on Directed Energy, Volume 1 (Directed Energy and Cloud Shadows)

Gail Vaucher and Michael Lee
DEVCOM Army Research Laboratory

Andrew Gatzke
United States Military Academy

REPORT DOCUMENTATION PAGE

1. REPORT DATE	2. REPORT TYPE	3. DATES COVERED START DATE	END DATE
January 2026	Technical Report	2024 Oct 1	2025 Sep 30

4. TITLE AND SUBTITLE
Environmental Impact on Directed Energy, Volume 1 (Directed Energy and Cloud Shadows)

5a. CONTRACT NUMBER	5b. GRANT NUMBER	5c. PROGRAM ELEMENT NUMBER
5d. PROJECT NUMBER	**5e. TASK NUMBER**	**5f. WORK UNIT NUMBER**

6. AUTHOR(S)
Gail Vaucher, Michael Lee, and Andrew Gatzke

7. PERFORMING ORGANIZATION NAME(S) AND ADDRESS(ES)	8. PERFORMING ORGANIZATION REPORT NUMBER
DEVCOM Army Research Laboratory ATTN: FCDD-RLA-ID White Sands Missile Range, NM 88002	ARL-TR-10254

9. SPONSORING/MONITORING AGENCY NAME(S) AND ADDRESS(ES)	10. SPONSOR/MONITOR'S ACRONYM(S)	11. SPONSOR/MONITOR'S REPORT NUMBER(S)

12. DISTRIBUTION/AVAILABILITY STATEMENT
DISTRIBUTION STATEMENT A. Approved for public release: distribution unlimited.

13. SUPPLEMENTARY NOTES
ORCID(s): Michael Lee, 0000-0002-0419-6069

14. ABSTRACT
Atmospheric cloud shadows have a positive and negative effect on "seeing" (image degradation due to atmospheric turbulence) and on coherent light propagation, such as that of a laser. To minimize visual or laser distortion, minimal density variations along an open-air propagation pathway are required. Unfortunately, the natural state of the atmosphere includes an abundance of density variations, which are characterized as optical turbulence via an index of refraction structure function (C_n^2) parameter. The highly turbulent atmosphere is largely fueled by solar radiation heating the soil, which creates an unstable environment. When a cloud shadow moves over an optical path, direct sunlight abruptly becomes diffuse. The sharp surface heat reduction inhibits vertical mixing, lowering C_n^2. This condition persists as long as the shadowed environment suppresses the buoyancy/thermal eddies. At the shadow's edge, C_n^2 sharply rises, due to the localized large thermal gradient (density variations). If a cloud shadow persists, favorable seeing continues until the heat released by the ground becomes trapped between the ground and cloud cover, such as in an overcast scenario. In this report, cross-discipline concepts (atmospheric, directed energy) are presented, followed by two representative cloud shadow cases (partly cloudy and overcast). The report concludes with a summary of an investigative modeling project that used machine learning techniques in constructing a 3-D cloud model from which cloud shadow mapping is anticipated.

15. SUBJECT TERMS
directed energy, clouds, cloud shadows, optical turbulence, atmospheric impacts, stability, C_n^2, Military Information Sciences

16. SECURITY CLASSIFICATION OF: a. REPORT	b. ABSTRACT	C. THIS PAGE	17. LIMITATION OF ABSTRACT	18. NUMBER OF PAGES
UNCLASSIFIED	UNCLASSIFIED	UNCLASSIFIED	UU	47

19a. NAME OF RESPONSIBLE PERSON	19b. PHONE NUMBER *(Include area code)*
Gail Vaucher	(520) 691-6169

STANDARD FORM 298 (REV. 5/2020)
Prescribed by ANSI Std. Z39.18

Contents

List of Figures

List of Tables

Acknowledgments

The authors wish to recognize Dr. William “Bill” Klein (Science and Technology Corporation) for the provision of optical turbulence and atmospheric data; and appreciation is extended to Dr. Cheryl Klipp (ARL) for her technical reviewer insights; and finally, a special thanks to ARL’s Technical Publishing group for its consistently excellent technical editing, specifically to team lead technical editor Jessica Schultheis.

1. Introduction

Improved "seeing" (image degradation due to atmospheric turbulence) conditions occur when there are minimal density variations along the viewed pathway. The same is true for energy that is emitted and transferred in a controlled direction, such as the coherent light of a laser.

In contrast, the greater the density variations, the more significant the effects on the traveling beam quality. Quantifying these atmospheric density variations is difficult, however; temperature is related to density such that it can be used to map iterative impacts culminating in a laser beam characterization at the target. While there are several destructive atmospheric elements to the propagating laser beam, an observed random influence along a beam path includes clouds and cloud shadows. Whether attempting to travel through the moist air of a cloud or traversing the quasi-random cloud shadows, the quality of laser energy is significantly impacted. In this report, a brief review of the high energy laser (HEL) and established atmospheric effects are provided. Built upon this foundation, the impacts of clouds and cloud shadows are described. Finally, experimental acquisition of cloud quantification and modeling of 3-D clouds for the purpose of laser applications are summarized.

2. Background

To understand impacts on laser propagation, one needs to first comprehend the energy source and the basic concepts associated with directed energy (DE). In this section, a very brief history of the laser and its operation sets the foundation.

2.1 Brief Laser History

The Light Amplification by Stimulated Emissions of Radiation, or LASER, began as a proposed process of stimulated emission by Albert Einstein in 1917. By the early 1960s, the first laser was created (a synthetic ruby laser) and laser research gradually evolved from the controlled laboratory environment to open-air devices (Hogan and Rose 2019).

With the atmosphere as the medium through which the laser propagated, environmental impacts were investigated, and aspects of the observed patterns were modeled. Manageable laser characteristics were harnessed and converted into productive tools having applications in multiple fields, such as communications, medicine, precision machinery, etc. (Hogan and Rose 2019).

2.2 Laser Basics

Lasers generate coherent light using a gain medium, with an energy source or pump to prompt photons traveling between two mirrors. As the photons traverse between the total and partial reflectors (mirrors), they become "in phase," so that when exiting the gain medium tube on the partial reflector side, the laser beam is coherent.

Lasers are typically characterized by the device type, weight, power, and/or size. Laser types can include solid state, semiconductor, liquid/dye, pulsed lasers, etc. For this investigation, the HEL type being addressed is a solid-state and/or pulsed laser.

Laser output manifests as a continuous wave or a pulsed wave. The continuous wave laser brings high energy to its end point but can be significantly impacted by the medium through which it travels (see Sections 3 and 4). The pulsed laser operates at a set duration rate and is less impacted by the medium due to the "cool down" period between pulses. The pulsed laser encounters other factors, which will be described in a future section.

2.3 HEL Operation

In this study, the solid and/or pulsed HEL operation is presumed to be outside, with the beam propagating through the Earth's open atmosphere. The HEL challenge is for the beam to travel from source to target, while retaining as much of the original coherent energy at the target. When the beam leaves the source, the beam director and beam control are typically characterized by the device's aperture diameter and beam jitter. Passing through the air, whether along a horizontal or slant path, the beam is described by the atmospheric conditions, the range of path, and the transmission. The HEL beam that arrives on target is quantified by power on the target, the beam spot size, and the impact on the target material.

2.4 Terms

DE is an energy type that emits and is transferred in a controlled direction. DE is typically in the form of electromagnetic radiation. HELs are a form of DE that can keep propagating its energy as long as it has electrical power.

3. Environmental (Chemical) Impacts on DE

The general HEL propagation through the open air results in repeatable beam distortions and is primarily a function of chemical and thermodynamic atmospheric characteristics. In this section, the chemical elements are addressed. These chemical elements can be grouped into two categories: nonlinear and linear impacts. Each category is described below.

3.1 Nonlinear Impacts

Nonlinear impacts include self-induced HEL beam spreading, distortion, and bending. These effects occur when HEL energy is absorbed by atmospheric molecular and aerosol constituents that in turn heat the air along the beam path, creating density or refractive index gradients, which distort and degrade the beam (Figure 1).

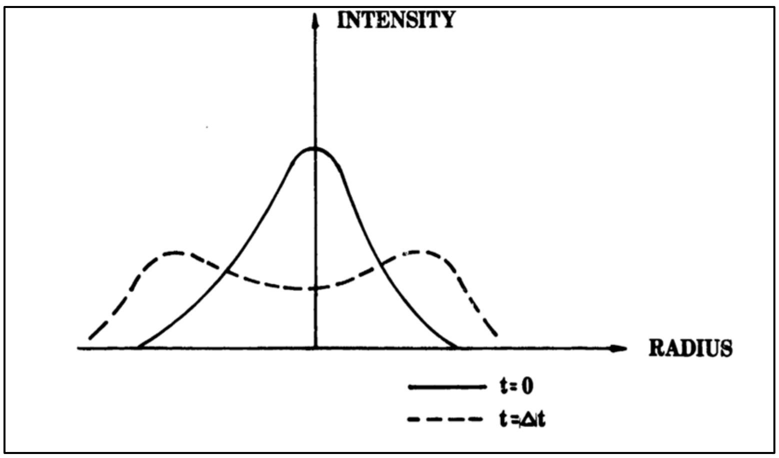

Figure 1. Nonlinear HEL effects (e.g., thermal blooming) result in self-induced beam intensity changes (Pries 1980).

The most important nonlinear effect is thermal blooming. This occurs when there is not enough ventilation along the beam path to remove the laser-heated air from the beam path. Consequently, the beam becomes distorted and defocused, as seen in the "no wind" case of Figure 1. Here, the irradiance is redistributed from a Gaussian shape into a donut shape, showing little to no energy at the beam center (aimpoint) (Pries 1980).

If the laser beam were slewed into cooler air, the beam would be deflected into the wind direction (cooler air) due to the index of refraction gradient and become effectively defocused. Under these conditions, the original circular HEL beam becomes a crescent shape on the upwind (cooler) side of the beam axis at the target.

Other nonlinear effects include thermal bending and bleaching. Bleaching occurs when the beam causes a decrease in molecular absorption by depleting the absorbing molecule supply.

3.2 Linear Impacts

Linear impacts include attenuation (reduction of beam intensity), beam spread, beam wander, and distortion. The attenuation stems from molecular and aerosol absorption and scattering. Beam wander and distortion are primarily from optical turbulence.

The major attenuation processes in the atmosphere are line absorption, continuum absorption, aerosol scattering, and aerosol absorption. There are two sources of continuum absorption that are important for the laser's infrared propagation: 1) the pressure-induced N_2 absorption band and 2) the water vapor continuum (Pries 1980).

3.2.1 Absorption/Scattering

Nearly all atmospheric absorption in the infrared is caused by H_2O, CO_2, O_3, CH_4, and N_2O. Fortunately, all but water (H_2O) and ozone (O_3) are well-mixed, so that their concentrations are a fixed fraction of the total air density. Since water and ozone are highly variable, concentrations for absorption calculations must be obtained through measurements (Pries 1980).

For the HEL, absorption and scattering are dependent on particle size distribution, number density, chemical composition, and path length. Examples of particles impacting propagation include haze, dust, soot, sea salt, volcanic ash, and hydrometeors (e.g., rain, fog, snow, and hail). Scaling particle radius versus wavelength associate Mie scattering with hail and Rayleigh scattering with raindrops, drizzle, and cloud droplets. Dust, smoke, and haze fall into a negligible scattering category, though through absorption can create colorful sunset/sunrises (Petty 2006).

Scintillation is another linear effect. However, due to its strong relevancy to the atmospheric cloud discussion, this effect will be described separately in the next section.

3.2.2 Optical Turbulence

Turbulence manifests as small, quasi-random swirls of air parcel movements, known as eddies. By the conservation of air mass, the air parcels leaving one area are always replaced by arriving air parcels. Characterizing the air parcels by their temperature, the net result is a heat flux. While the transference of heat would qualify this attribute as a thermodynamic impact, the mechanism for these linear effects is still at the chemical/molecular level, so its description is initiated here.

Equating air temperature and density variations, when the laser beam encounters an eddy (optical turbulence), it bends toward the "cooler," more dense environment. This response cascades into phase distortions/incoherencies, as seen in Figure 2 (Pries 1980). While the beam does not attenuate, it does cause an energy redistribution resulting in fluctuations in the time and space. The net result is a function of the HEL wave size versus eddy size, and/or the pattern of warm/cold air pockets encountered.

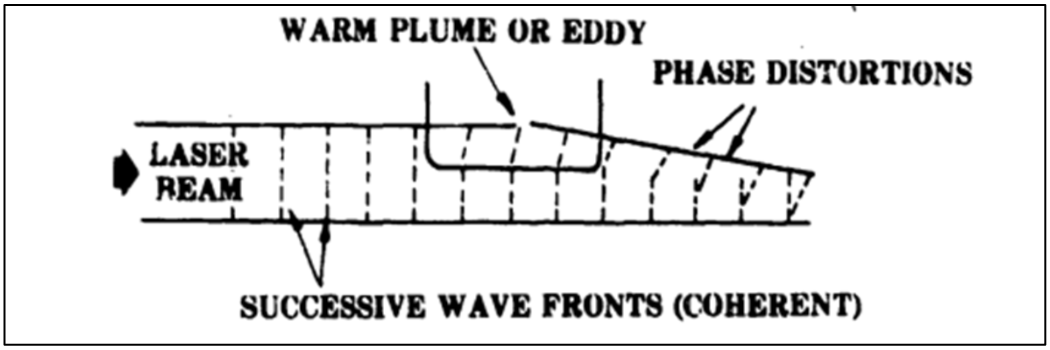

Figure 2. Laser interacting with an eddy (Pries 1980).

For example, if the eddies are larger than the HEL beam diameter, then the result will be a wandering beam at the target site. If the eddies are smaller than the HEL beam diameter, the net result at the target is beam spread. Finally, if there are pockets of hot/cold air traversing the beam (i.e., convection off a hot surface), the beam will appear to fluctuate in time, or twinkle (a.k.a., scintillate). These three scenarios are captured in Figure 3.

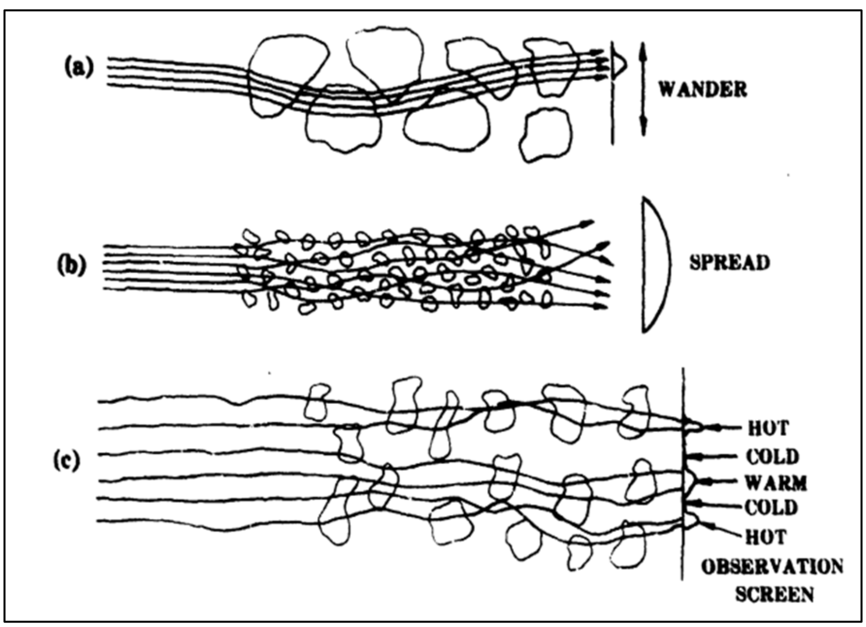

Figure 3. Eddy affects beam propagation: (a) eddy > beam diameter, (b) eddy < beam diameter, (c) scintillation (Pries 1980).

For scaling purposes, the atmospheric index of refraction is 1.0003, almost 1. According to Pries (1980), fluctuations of only 1% in the residual beam are sufficient to produce laser beam spread, wander, and scintillations. This result is due to the atmospheric turbulent dynamics and the accumulation of refractive anomalies along the optical path.

3.2.3 Quantifying Optical Turbulence

Quantifying this optical turbulence requires measuring the density or index of refraction variations. As mentioned earlier, these refractive indices redistribute the traveling energy of the laser beam, resulting in temporal and spatial fluctuations. The fluctuations cause the beam to bend/distort slightly as it progresses. While water vapor contributes to the fluctuations, temperature is the dominant factor. The scale of these variations is such that to quantify the changes requires a statistical parameter—namely, the index of refraction structure function, or C_n^2. This ensemble average is represented mathematically as

$$C_n^2 = \frac{\langle<(n_2 - n_1)^2>\rangle}{r^{2/3}} \tag{1}$$

where n is the index of refraction, and r is the distance between n_2 and n_1 (Walters and Kunkel 1981). C_n^2 is closely related to the temperature structure parameter, C_T^2.

$$C_T^2 = \frac{\langle<(T_2 - T_1)^2>\rangle}{r^{2/3}} \tag{2}$$

To complete the temperature versus index of refraction relationship:

$$n - 1 = (79 \times 10^{-6}) * P/T \tag{3}$$

where P is pressure, and T is temperature. The temperature structure function, C_T^2, is then related to C_n^2 (Tatarski 1961).

$$C_n^2 = ((79 \times 10^{-6}) * P/T^2)^2 * C_T^2 \tag{4}$$

Examples of the C_n^2 will be given in the next section.

4. Environmental (Thermodynamic) Impacts on DE

Optical turbulence primarily manifests on the molecular scale; however, for laser impact analyses and forecasting purposes, cause and effects are examined in the context of atmospheric thermodynamics. To best capture the processes, this context is examined temporally and spatially. Temporally, atmospheric thermodynamics manifest as systematic, diurnal atmospheric cycles. The spatial perspective focuses on specific thermodynamic products—namely, clear, overcast, and partly cloudy sky conditions.

4.1 Temporal Thermodynamic Impacts

The thermodynamic influence on DE stems from solar energy. Starting on an astronomical scale, the Earth's atmosphere is powered by solar energy. Shortwave radiation from the sun propagates through space to the Earth, 24 h/day, 7 days/week (24/7). Upon reaching the Earth, solar radiation is scattered, absorbed, and transmitted as it traverses from the top of the atmosphere to the surface. Air motion (winds) across the rotating planet's surface is driven by the differential solar heating of the ground. The Earth's tilt and orbit around the sun create a seasonal energy distribution. The seasonal trends are the cumulative effects of persistent diurnal cycles. It is within these diurnal cycles that repeatable constructive and destructive impacts on laser propagation are found.

To capture the net effects on DE, the diurnal cycle is described from three different angles. First, the solar energy that drives the cycle is summarized. Second, the cycle is explained as a function of a surface, vertical temperature gradient referencing the meteorological terms of unstable, neutral, and stable environments. Finally, optical turbulence (C_n^2) is correlated with stability and solar energy cycles. For each perspective, the following are presumed:

- The atmospheric area being considered is the surface layer, or the first 100 m above ground level (AGL);
- The Earth's surface for the given generic case is flat, open desert terrain (no foliage canopy to interrupt sunlight); and
- The sky condition is persistently clear (no clouds, fog, haze or smoke).

4.1.1 Diurnal Cycle: Solar Energy

The diurnal cycle starts at (1) sunrise, when energy from the sun projects onto the Earth's surface, causing the ground to warm. As the sun rises higher in the sky, the Earth's surface continues to warm until the sun reaches its zenith or highest position in the sky dome, which is also known as (2) solar noon. (3) Continuing past solar noon, the sun progresses through the western sky, still warming the ground, however, with systematically less radiation, until finally (4) the sun sets below the western horizon. The wax and wane of solar energy reaching the ground during these daylight time periods are largely a function of the number of atmospheres the energy must travel through before it reaches the surface. At solar noon, energy travels through 1 atmosphere (atm). Around sunrise and sunset, it must traverse at least 29 atm. The diurnal thermal cycle does not end at sundown. Continuing without a direct heat source, (5) the ground radiates longwave radiation/heat throughout the nighttime until once again, the sun projects its shortwave radiation on to the Earth's surface. And the cycle resumes.

4.1.2 Diurnal Cycle: Atmospheric Stability

Atmospheric stability is defined by an air parcel's buoyancy with respect to its hydrostatic equilibrium or vertical displacement. The three stability terms relevant to this study include *unstable*, *neutral*, and *stable*.

When a vertical temperature profile reports near-surface values warmer than those aloft, this condition is called "unstable," or positively buoyant, due to the warmer surface air parcels wanting to rise to their level of equilibrium (level of the same temperature). When the vertical temperature profile indicates surface magnitudes are cooler than those aloft, the atmosphere is considered "stable" or negatively buoyant. That is, the air parcels near the surface are wanting to sink to their zero buoyant condition (level of same temperature). Neutral conditions or zero buoyant forces occur when the environment is isothermal. Figure 4 demonstrates these three vertical temperature profiles. Note that in the troposphere, temperature naturally decreases with height at an adiabatic lapse rate of –9.8 K/km. This is graphically represented by the left sloped temperature curve above the surface.

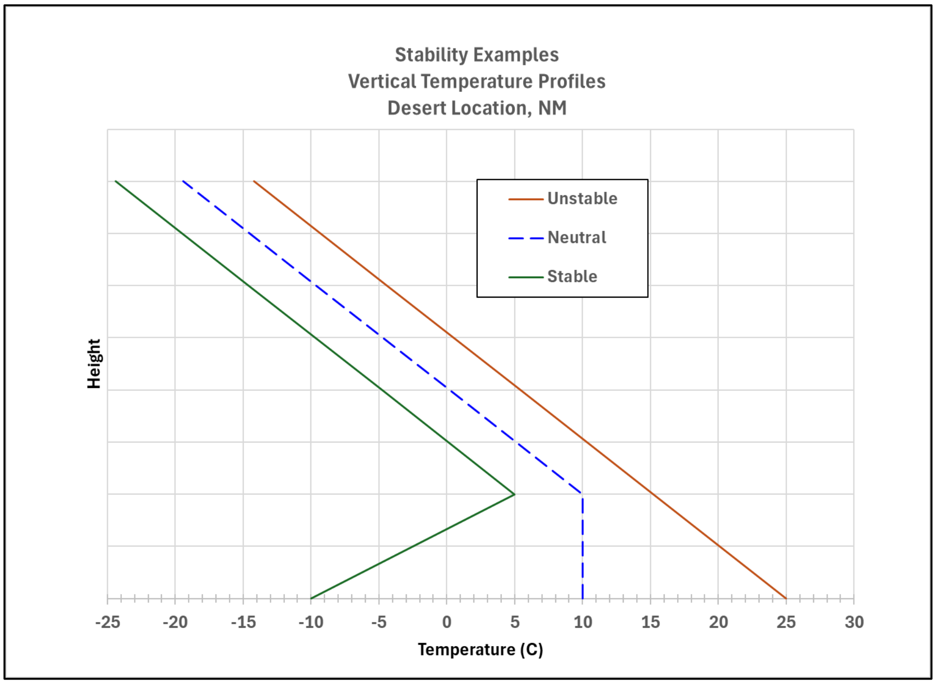

Figure 4. Examples of unstable, neutral, and stable atmospheric temperature profiles.

(Stability can also be envisioned using a pot of water sitting on a stove. When the stove is turned on, the heat at the base of the pot warms the water. Unstable conditions manifest as warm water rises to the surface, eventually coming to a boil. Stable conditions occur when there is no heat under the pan, and the water is stagnant/laminar. A neutral state occurs when the pan and the water have the same temperature.)

Assimilating the three stability states (*unstable*, *neutral*, and *stable*) with the diurnal solar energy cycle of Section 4.1:

(1) Shortly after sunrise, the solar energy warms the Earth's surface, and the atmosphere reports *unstable* conditions. These continue through (2) solar noon, (3) the afternoon, and until shortly before (about 40 min) sunset, when the atmosphere becomes *neutral* (isothermal) near the surface. (4) Once the sun drops below the western horizon, (5) longwave radiation (heat) is released from the ground. This continues throughout the night, resulting in cooler surface temperatures than those aloft or *stable* conditions. When the sun rises, the near-surface atmosphere takes about an hour of warming to reach an isothermal (*neutral*) state, after which the projection of persistent solar shortwave radiation onto the Earth's surface results in *unstable* daytime conditions. And the cycle resumes.

To more easily discern stability, a delta-temperature (ΔT) parameter is calculated using

$$\Delta T = T_{16m} - T_{2m}. \quad (5)$$

Here, unstable conditions (warm air under cooler air) result in negative ΔT values. Positive ΔT values indicate a stable environment (cooler air under warmer air). The environment is neutral, when ΔT equals zero (isothermal).

4.1.3 Diurnal Cycle: Optical Turbulence

Optical turbulence is very sensitive to temperature variations, even very small differences. In earlier sections, temperature was mapped to density in the atmosphere, enabling optical turbulence to be a function of temperature variations. It follows then that a diurnal optical turbulence pattern (C_n^2) would track similarly to those of the solar and stability cycles.

Given the partly cloudy case shown in Figure 5, concurrent solar radiation, ΔT, and C_n^2 time series are displayed. (Additional 2001 March 24 atmospheric summary information is shown in Appendix A.) For this case, the day starts clear of clouds, as seen with the solar radiation time series smoothly increasing at a relatively steady pace until about 1100 LT. Between 1100 and 1500 LT, clouds randomly reduce the incoming solar radiation, as seen in the downward blue data spikes. From around 1500 to shortly before sunset, the radiation systematically decreases until it reaches 0 W/m^2. For the nighttime hours, solar radiation registers 0 W/m^2. Coinciding with nighttime periods, the ΔT (green) reports stable or positive values. Daytime ΔTs show unstable or negative magnitudes. The only neutral events occur during the thermal cross-over between these two conditions—namely, around 1 h after sunrise and about 40 min before sunset.

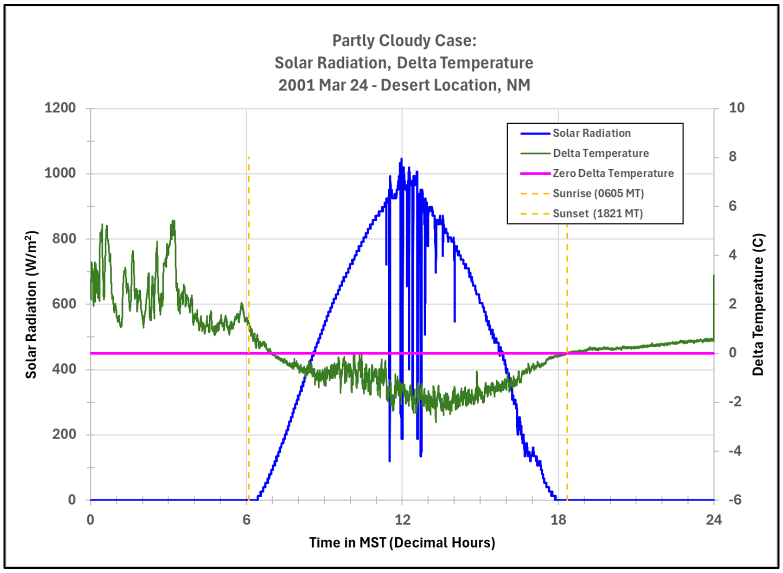

Figure 5. 2001 Mar 24: diurnal thermal cycles.

Figure 6 shows two reciprocal-path C_n^2 measurements sampled concurrently with the Figure 5 data. Due to the difficulty in sampling C_n^2, reciprocal horizontal path measurements were used to ensure a perpetual relative calibration between the given sensors. That is, while one scintillometer sampled the horizontal atmospheric path from the 0-km tower to the 1-km tower at 8 m AGL, a second independent scintillometer sampled the same optical turbulence from the 1-km tower to the 0-km tower at 8 m AGL.

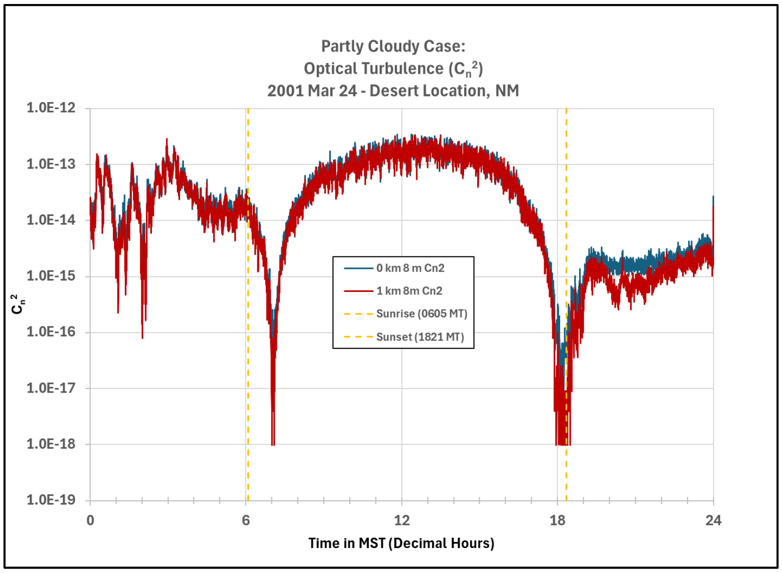

Figure 6. 2001 Mar 24: diurnal optical turbulence cycle.

To help visually align the time series, sunrise and sunset times are labeled on both plots. The Mar 24 case was selected due to its proximity with the annual spring equinox (equal sunlight and darkness over a 24-h period). During daylight hours, C_n^2 magnitudes (10^{-12} to 10^{-13}) report high optically turbulent environments, whereas the lowest C_n^2 values (10^{-18}) coincide with the neutral events. In between these extremes are a mix of *stable* (primarily nighttime) and *unstable* (drainage flow mixing overnight) environments.

In terms of HEL applications, these patterns show that daytime heating (unstable conditions) have the greatest disruptive impact on the beam performance due to excessive turbulence, whereas the “best” beam-on-target time periods occur during neutral conditions. When testing laser beam quality in an open-air environment, neutral events are a prime time for minimizing atmospheric impacts on a laser’s performance.

From independent studies regarding neutral events, these conditions can be extended due to ground moisture and cloud cover. In the next section, clouds and their DE impacts will be described.

4.2 Spatial Thermodynamic Impacts

The ideal HEL propagation environments have no density variations along the HEL beam path. As such, the beam-on-target would be strictly a function of the laser technology. Atmospherically speaking, conditions for this ideal scenario occur twice a day, during neutral atmospheric conditions.

From other studies (Vaucher and Raby 2013), neutral atmospheric conditions are forecastable and can produce significantly improved seeing conditions for long-range imaging. Figures 7 and 8 show the impact of turbulence as a function of visible light. Both images were taken on the same day, from the same location, viewing a 2.6-km path using the same camera. Only the time of day was changed. The turbulent mid-afternoon (1432 Mountain Standard Time [MST]) effects of Figure 7 blur image edges, much like a HEL beam would experience. These inhibitions are removed once the atmosphere takes on the isothermal (minimal density variations) "neutral event" conditions at 1703 MST. In Figure 8, object edges are sharp and colors distinct.

Figure 7. High turbulence (unstable): 2.6-km desert path (2013 Feb 5, 1432 MST).

Figure 8. Low turbulence (neutral): 2.6-km desert path (2013 Feb 5, 1703 MST).

HEL paths with minimal density variables can also occur during passive stable and, in special cases, lightly unstable conditions.

The most interruptive atmospheric conditions for HEL propagation are associated with the unstable daytime environment. Perhaps it is somewhat ironic that the disruptive nature of an unstable atmosphere is also the requirement for building large cumulus clouds, whose shadows can then generate improved HEL propagation conditions.

In the next section, clouds and their potential for improving HEL performance are addressed.

4.2.1 Cloud Types and Shadows

There are three basic cloud types: high clouds (i.e., cirrus), mid-level (i.e., stratus), and low level (i.e., cumulus). All three cast shadows on the Earth's surface and/or lower clouds. However, their net impact varies as a function of the cloud filtering effects.

Cirrus clouds are typically quasi-transparent and shaped as long in length and thin in width. Their limited net solar radiation reduction gives little improvement on daytime DE applications. However, the sun's energy transmitting through cirrus clouds just after sunrise can delay and, in some cases, elongate the sunrise neutral event. Solar energy from a setting sun can create neutral conditions earlier than a clear sky would.

Stratus cloud cover can be extensive in terms of obscuring the sky dome. These clouds are formed in statically stable air and are passive in that buoyant forces suppress vertical growth. They are not turbulently coupled with the underlying surface. Thus, the non-convective stratus clouds tend to create improved HEL atmospheric conditions by virtue of the cloud formation, not necessarily its shadow.

Cumuliform clouds are formed in statically unstable air. Their vertical growth is enhanced by the buoyant forces bubbling up from the surface. This rising warm air continues until it reaches a level of condensation. The level of condensation serves as the cloud's base. Air parcels continue to rise within the cloud forming a cauliflower-shaped appearance, while the air parcels reach equilibrium. As additional warm, moist air rises, the cloud density increases, becoming more opaque. Most cumuliform cloud diameters are roughly equal to their heights above the ground. The net effect is a cloud that is able to project a shadow on the Earth's surface (Figure 9).

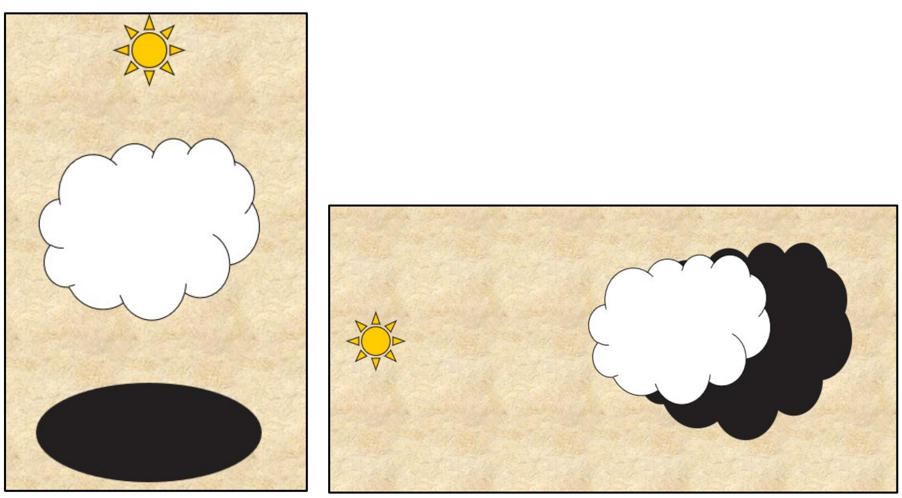

Figure 9. Zenith and angled cloud shadows.

The significance of having a cloud shadow is that due to the absence of direct sunlight, the diffuse radiation does not warm the ground as quickly. Thus, the shadows represent cooler environments to those in direct sunlight. This implies that the strength of turbulence generated is reduced, creating a more favorable environment for HEL propagation. In the next section, mapping cloud shadows to better analyze HEL performance is presented.

4.2.2 Mapping Cloud Shadows

Quantifying in situ cloud shadows and their impact on optical turbulence is not trivial. Typical cloud shadowing studies utilize satellite data and the given projected occultation of sunlight onto the ground (Amin et al. 2013). As part of the core research application, only in-situ data resources were considered. Therefore, this spatial cloud shadow mapping technique looked toward only on-site measurements. The two relevant measurements sampled included whole sky imager (WSI) images and pyranometer data. The WSI method will be discussed in Section 5. In this section, contoured pyranometer data are demonstrated as tools to approximate cloud perimeters. Simulating solar radiation data over a random field, Figure 10 shows contoured solar radiation gradients. As will be shown in the next section, cloud shadows can cause solar radiation magnitude drops of 50% or more, over a 10-s period. Interpreting Figure 10 data, the simulated 800 W/m^2 values indicate unobstructed solar radiation reaching the sensor; however, the concentric 400 W/m^2 lines frame a cloud shadow. Within the interpolated gradient is the cloud edge. This transitional zone sports a significantly turbulent environment, as the full throttle heating of direct sunlight sharply mixes with the subdued environment of diffuse energy. For concept purposes, the contours are colored such that the outer edge (representing direct sunlight) uses colors associated with sunlight (orange and yellow), and the shadowed area uses the darker blue and purples.

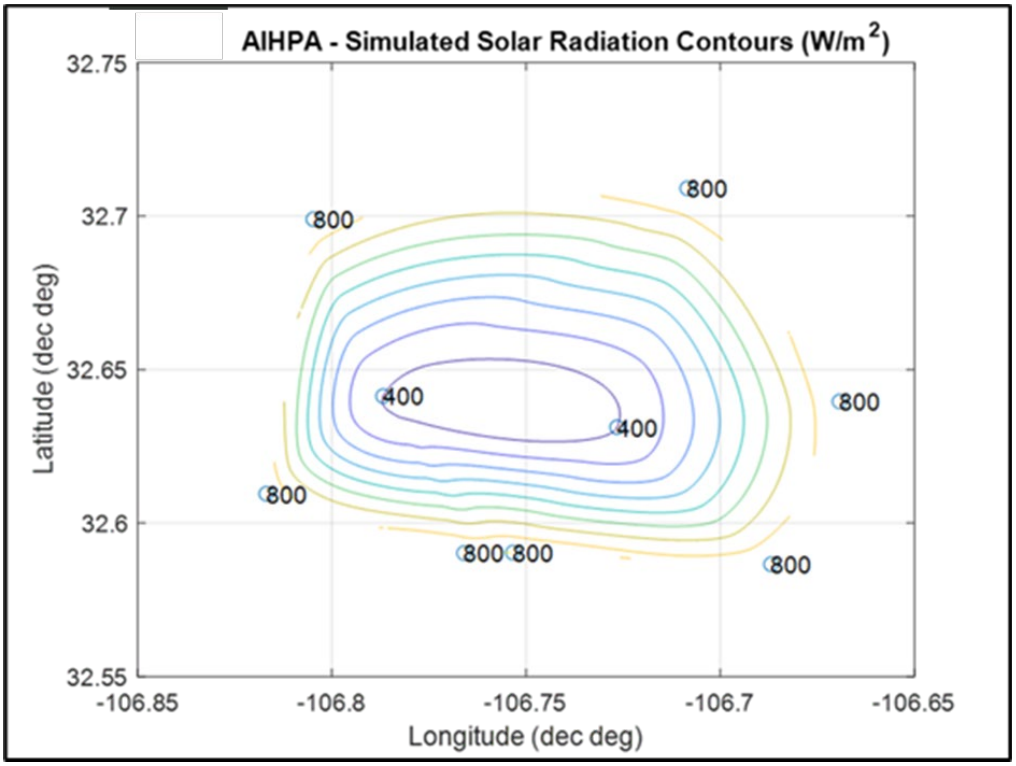

Figure 10. Simulated contour plot of solar radiation over a random area.

Presuming the cloud type includes movement, a sequence of three graphs (Figure 11) demonstrate how the solar radiation measurements across a horizontal field could track the cloud movement. Understanding that the cumulus cloud type being simulated is 4-D, in that the cloud is always growing or decaying in the vertical, the shape of the contours adapts to the evolving perimeter of this dynamic solar occulter.

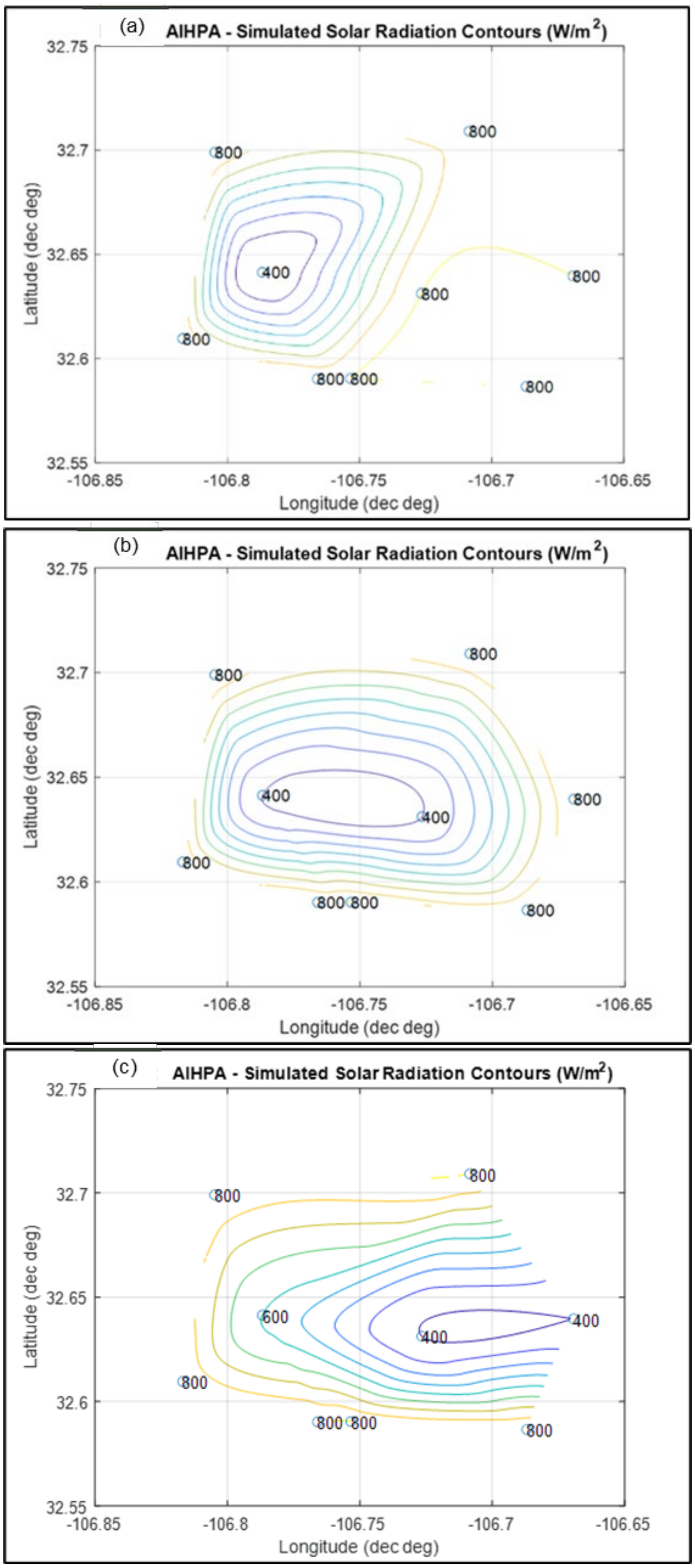

Figure 11. Sequenced (a, b, c) contours show left→right cloud motion.

5. Cloud Shadow Effects on Optical Turbulence

The cloud shadow effects are best understood starting with the previously described baseline of unobstructed solar energy reaching the Earth's surface. This atmospherically unstable environment near the surface produces an optically turbulence environment (high C_n^2 values). The most significant cloud shadow impact on HEL propagation begins with a sudden, severe drop in insolation that cascades into a reduction of optical turbulence. From a fixed site, the highly energized incoming solar radiation reaching the surface suddenly (within seconds) drops by over 50% due to a cloud occulting the direct solar radiation. This leaves only diffuse energy to warm the same ground. The sharp reduction of surface heat results in cooler air just above the Earth's surface, inhibiting the vertical mixing (thermal plumes and eddies) of the former unstable environment. The more laminar condition created is generally associated with stable environments. The lack of convective mechanical turbulence lowers the C_n^2 within the shadowed area. The condition persists as long as the shadow environment suppresses the buoyancy/thermal eddies. The magnitude of reduction is a function of the cloud opacity, the duration of the shadow, and the solar radiation just outside the shadow.

Cloud shadow edges are worthy of note in that the sharp temperature differences between the direct and diffuse sunlight conditions produce wind shear, leading to mechanical turbulence. This localized and often transient condition can temporarily increase optical turbulence C_n^2 at the shadow boundary.

Quantifying these cloud shadow effects on optical turbulence can be done using concurrent measurements. In the next subsections, two 24-h (single-day) cases quantitatively demonstrate the effects observed under partly cloudy and overcast conditions.

When associating measurements with the cloud shadow impact concepts, it is important to note that the measured C_n^2 values represent a horizontal volume of air 8 m AGL and 1 km long. The delta temperatures are single location samples taken at mid-path (500 m) and calculated from temperatures that bracket the C_n^2 horizontal path—sampling 8 m above the path at 16 m AGL and 6 m below the path (2 m AGL). The solar radiation measurements are sampled only at the end of the 1-km path, which we will call "Site B." Cloud edges, when abrupt, can fall anywhere between the start/end of the 1-km pathway. To quantitatively witness these interfaces, the edge needs to cross sensor locations at the 500-m (delta temperature) and Site B (solar radiation) locations; or they can be numerically seen as a more gross, net effect along the 1-km pathway via the C_n^2 values.

5.1 Partly Cloudy Sky Impacts Optical Turbulence

The partly cloudy case chosen is displayed in Figures 5 and 6. These data were sampled from a high elevation (~4000 ft ASL) in the southern New Mexico desert. As a review, when analyzing C_n^2 time series, cloud shadows manifest as distinct dips or reductions in optical turbulence (see Section 4.1.3), often followed by potential upward spikes at the shadow edges. For this 2001 Mar 24 partly cloudy case, the day begins and ends with clear sky. Cumulus-type clouds appear midday. Figure 12 extracts just the partly cloudy solar radiation portion of this case study. The persistent daytime atmospheric condition midway along the HEL pathway is unstable, as seen in the coincident green delta-temperature time series.

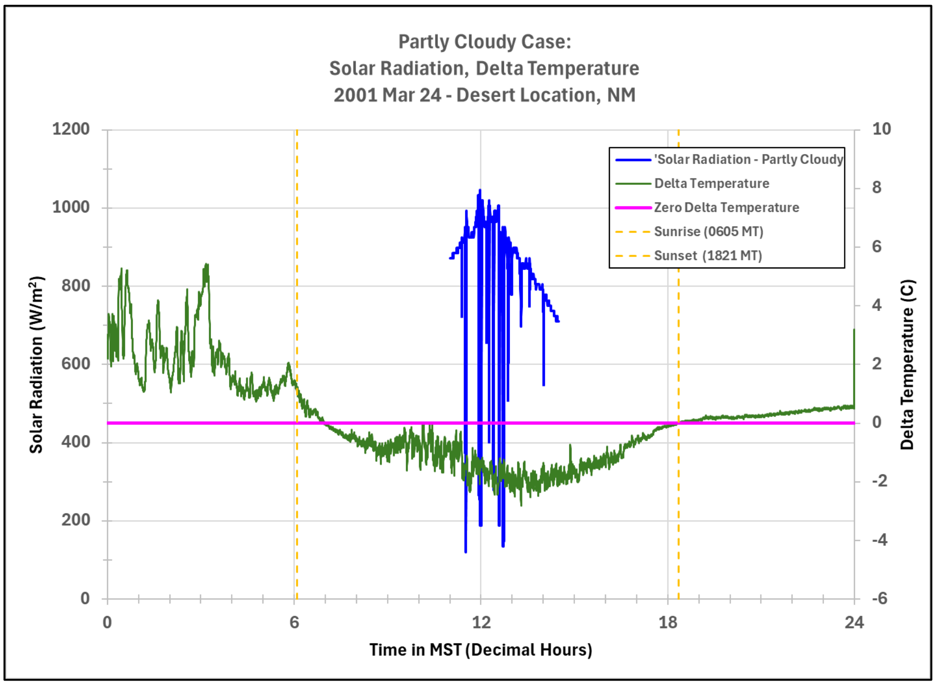

Figure 12. 2001 Mar 24: partly cloudy portion (thermodynamic variables).

Figure 13 focuses on the solar radiation and optical turbulence (C_n^2) measurements between 1100 and 1430 MST. The magnitude of the large solar radiation changes is notated with black triangles, which are scaled on the left y-axis. Only those differences that were greater than 100 W/m^2 are marked on the plot. A contrast between cloud events and the natural systematic waning of the afternoon sun can be discerned within this extracted data sample. That is, the optical turbulence shows a consistent trend after 1300 MST toward lower turbulence as the sun's energy must traverse additional atmospheres to reach the Earth's surface.

Focusing on the midday cloud events, the greatest single step solar radiation change in this example was 670.5 W/m^2, which occurred between 12:00:40 MST (348.66

W/m^2) and 12:00:50 MST (1019.16 W/m^2). This 192% increase in solar energy over a 10-s period is not uncommon when a site exits a cloud shadow into direct sunlight.

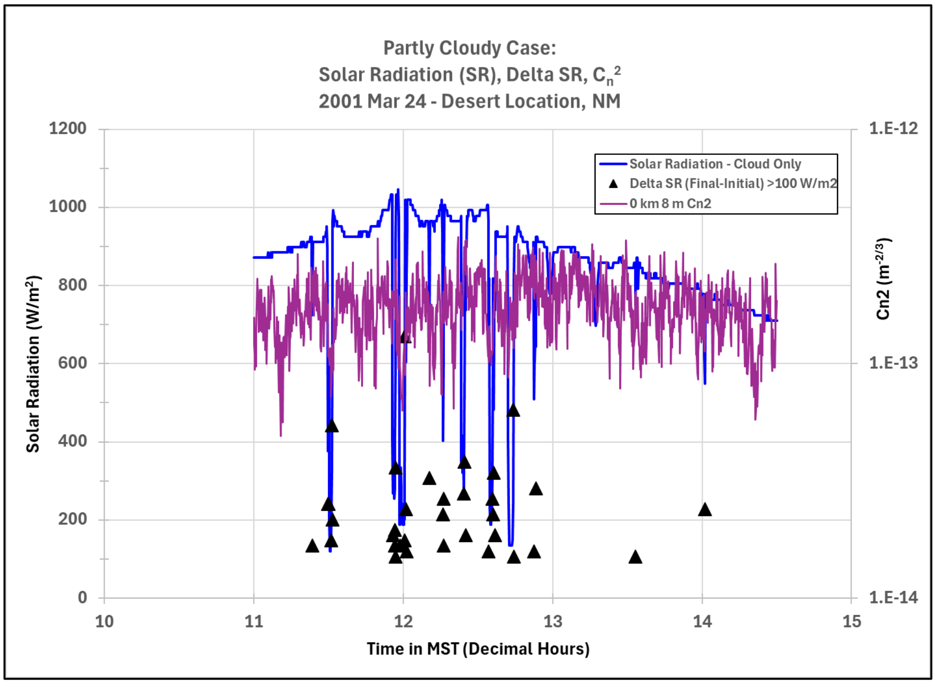

Figure 13. 2001 Mar 24: partly cloudy (midday clouds/turbulence).

Examining this same cloud event more closely, the initial cloud signature is noted 2 min earlier, as seen in Table 1. The "full sun" solar radiation started above 1000 W/m^2. Then, over a period of 30 s, the occulting cloud deprived the 1-km location of direct sunlight, reducing the insolation by 82%. Radiation values hovered over the 180–300 W/m^2 range while the cloud shadow persisted. Two minutes later, however, irradiance values return to their above 1000 W/m^2 status. The greatest boost of solar energy occurred over a period of 10 s, as discussed earlier.

Table 1. 2001 Mar 24: midday cloud event.

Time			Solar Radiation	Optical	Turbulence
Hour	Minute	Seconds	(W/m2)	Cn2-0km	Cn2-1km
11	58	0	1045.98	9.55E-14	7.78E-14
11	58	10	978.93	1.29E-13	1.04E-13
11	58	20	455.94	1.62E-13	1.12E-13
11	58	30	187.74	1.94E-13	9.42E-14
***	***	***	***	***	***
12	0	10	187.74	1.08E-13	1.30E-13
12	0	20	214.56	1.18E-13	7.90E-14
12	0	30	201.15	9.73E-14	9.80E-14
12	0	40	348.66	8.94E-14	1.44E-13
12	0	50	1019.16	1.70E-13	1.36E-13

Examining the correlated optical turbulence measurements, the preliminary impact of these volume (vs. point) measurements is gleaned by a visual inspection of the time series trends. The isolated numerical changes are less obvious, which is where understanding how and where the sampling occurred is critical. For example, in Figure 14, the midday cloud event aligns with a temporary reduction of optical turbulence. Most of the other cloud events displayed also have temporarily reduced C_n^2 magnitudes associated with the same time period.

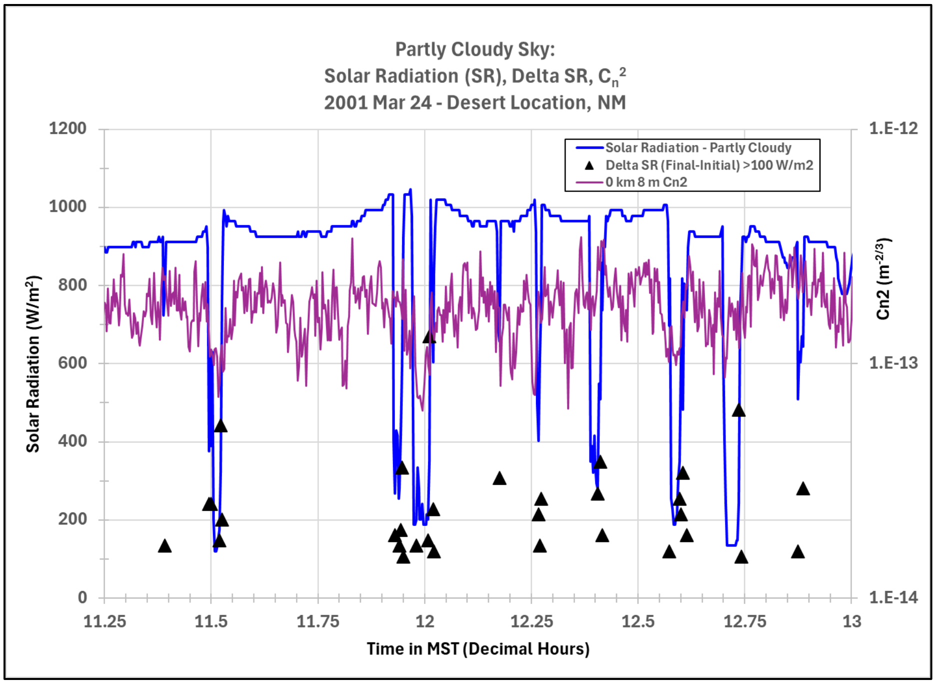

Figure 14. **2001 Mar 24: partly cloudy (enlarged midday clouds/turbulence).**

Occasionally, the cloud shadow timing is skewed, such as the 12.17 and 12.25 MST events shown in Figure 15. In the 12.17 MST case, the solar radiation located at Site B (the 1-km site) picked up the cloud cover before the 0- to 1-km C_n^2 sensor recorded its effect. In contrast, the 12.25 MST case shows the solar radiation drop after the C_n^2 magnitudes report a downward spike. For this latter event, it is likely that the 0- to 0.5-km path area received the shadow first, before it reached the pyranometer located at Site B (1-km position). Both examples reinforce the critical need of including sensor measurement context in such an analysis.

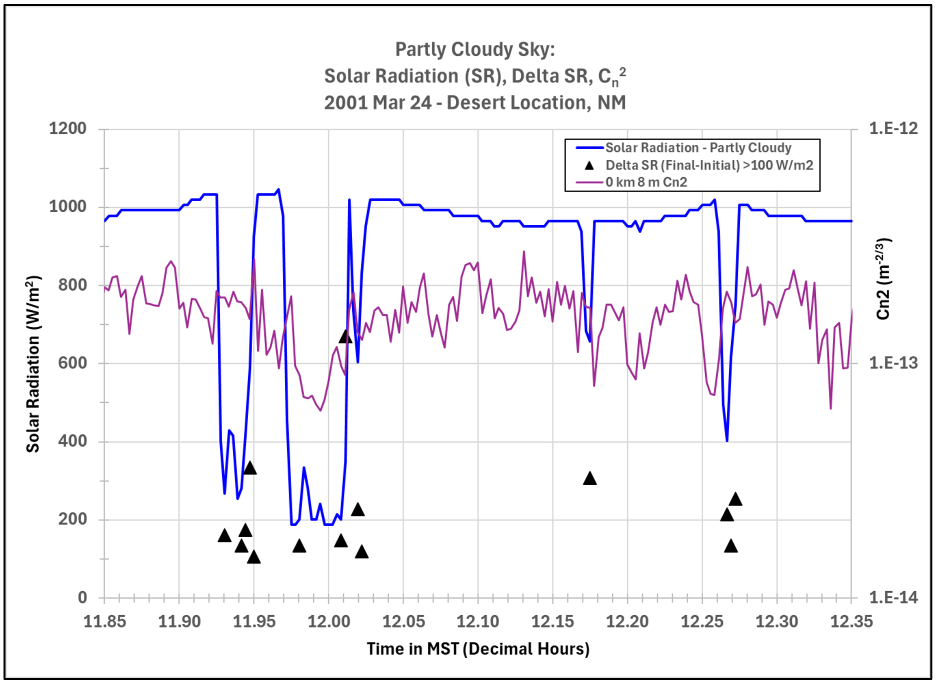

Figure 15. 2001 Mar 24: partly cloudy (extra-enlarged midday clouds/turbulence).

5.2 Overcast Sky Impacts Optical Turbulence

The second cloud shadow impact demonstration examines the effects of persistent cloud shadowing or overcast conditions. The selected case occurred on 2001 June 07 over the same southern New Mexico desert as the partly cloudy case. The 24-h weather conditions would be characterized as a "monsoon" pattern. That is, clear sky initiated the day, followed by partly cloudy and finally overcast with rain. Figures 16 and 17 show the concurrent 2001 June 7 thermodynamic and optical turbulence measurements, respectively. Sunrise and sunset are included to assist with the visual alignment between the two time series plots. For additional 2001 June 07 atmospheric summary information, see Appendix B.

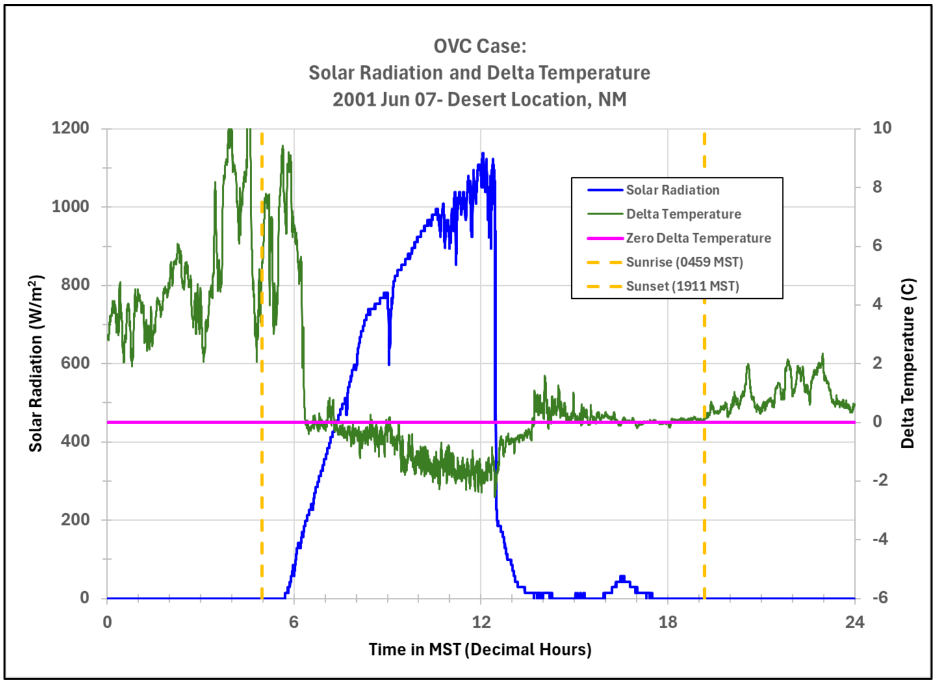

Figure 16. 2001 June 07: overcast case (thermodynamic variables).

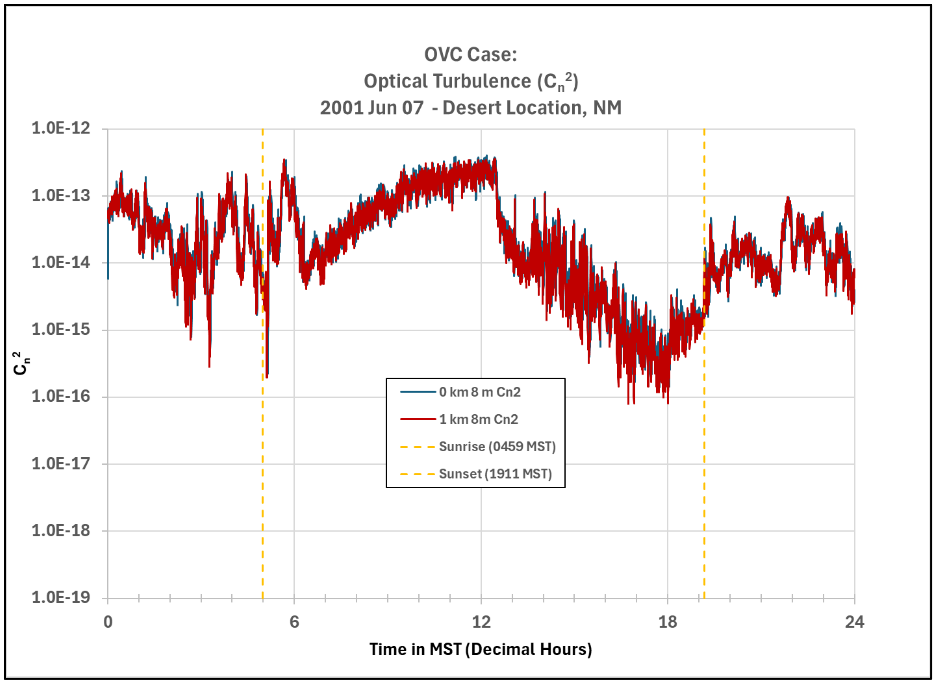

Figure 17. 2001 June 07: overcast case (optical turbulence).

As expected, the clear sky daytime hours report unstable temperature profiles (negative delta temperatures). The pre-dawn nighttime delta-temperatures indicate very stable conditions, and after sundown the stable environment is closer to neutral conditions. It is interesting to note that the stable pre-dawn periods are associated with improved optical turbulence conditions, though their inconsistency indicates that other factors, such as local mixing or drainage flow, perpetuate a variegated density variation along the 1-km pathway. The daylight hours, beginning at the sunrise neutral event, reinforce the expected optical turbulence dip (sunrise neutral event) followed by a normal clear (and near clear) sky increase in C_n^2. Shortly before 1100 MST, cloud signatures are observed in the solar radiation.

There is still enough incoming solar radiation to map a local solar noon (~1203 MST); however, by 1230 MST thick clouds over the 1-km site deprive the subject location of direct sunlight (Figure 18). The over 80% drop in solar energy reaching the surface is correlated with a gradual shift in the atmospheric stability and a gradual and persistent systematic optical turbulence reduction, as seen in Figure 19.

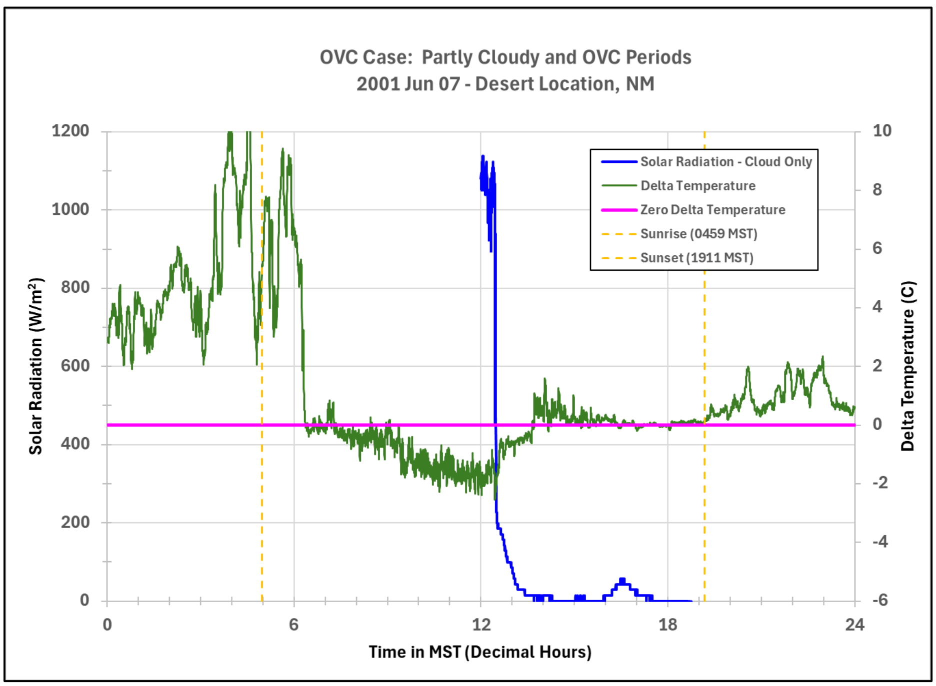

Figure 18. **2001 June 07: overcast portion (thermodynamic variables).**

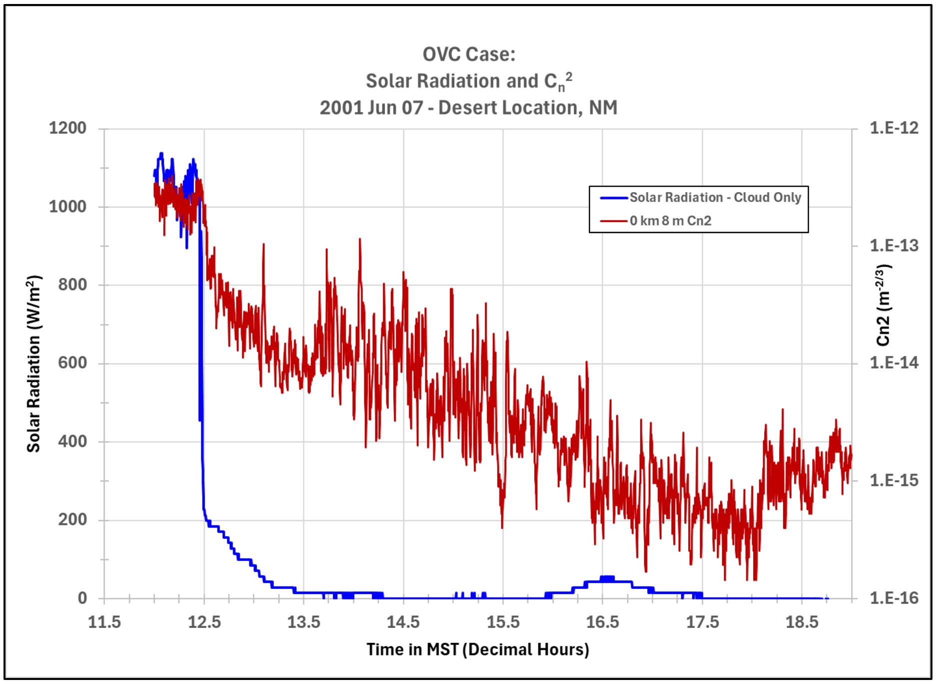

Figure 19. 2001 June 07: overcast portion (optical turbulence).

The C_n^2 shift from the 10^{-13} to 10^{-14} decade is reached after an hour of persistent overcast conditions. This length of time is needed to release the abundance of surface heat fueling the unstable conditions. Figure 20 shows a higher resolution plot between 1200 and 1500 MST.

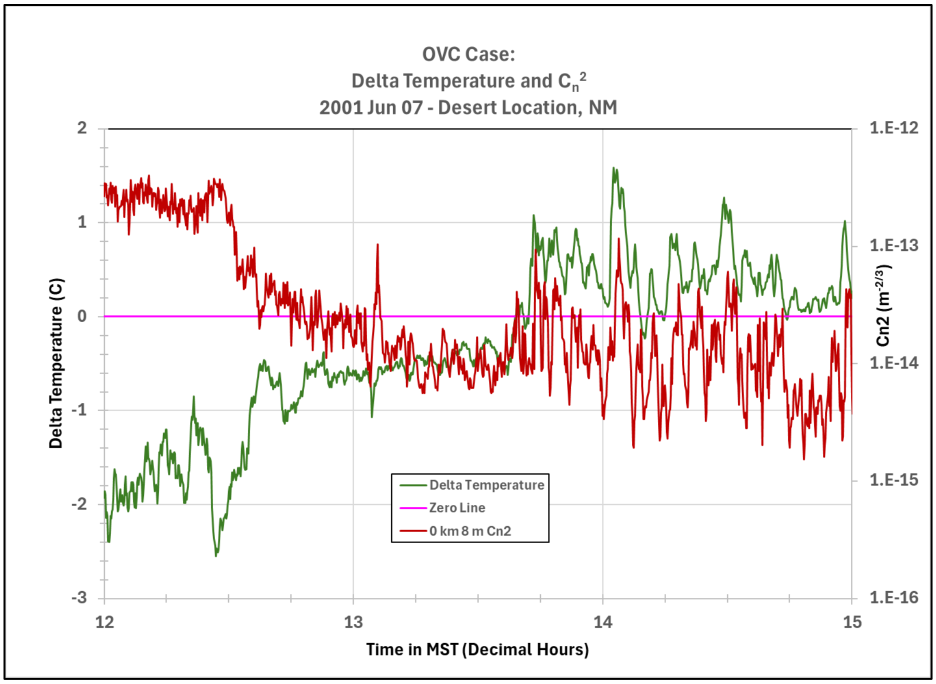

Figure 20. 2001 June 07: overcast portion (enlarged time series).

While the delta temperatures of Figure 20 are unstable, the oscillating natures of the delta temperatures and optical turbulence appear to mirror one another, albeit having different amplitudes. This is particularly evident during the short period of sustained solar radiation shortly after 1300 MST, which cascades into an upward spike in the optical turbulence and a shorter downward spike in the delta temperature.

Once the environment becomes neutral, that delta temperature/optical turbulence pattern changes to one where the two variables track the oscillations (Figure 20). The low solar energy yields a stable atmosphere that is near neutral, supporting persistently low optical turbulence magnitudes until about 1 h before sundown. As sundown approaches, the near neutral stability is correlated with increasing optical turbulence. This change is likely a function of local forcing created by the local rain events, ground moisture, significantly reduced insolation, and the effects of having a cloud blanket overhead. Without the cloud deck, the surplus of long wave ground radiation would create a cooler environment near the surface. However, with the clouds overhead, the long-wave radiation (ground warmth) is trapped within the local surface layer, leading to heightened optical turbulence.

5.3 Benefits of 3-D Cloud Model

Several points can be gleaned from these two sample cases. First, cloud shadows prompt areas of lower temperatures. While the cloud edges are optically turbulent (sometimes with an increase in optical turbulence), the persistently shaded surface areas created by cloud shadows favor reduced convection and lower optical turbulence. Second, the longer the duration of the shadow, the greater the opportunity for lower optical turbulences (improved seeing conditions), as seen in the mid-afternoon overcast case.

Third, cloud type is associated with cloud thickness, which impacts how much solar radiation reaches the surface. While convection/turbulence is needed to create cumulus clouds, the shadow cast over the surface by a mature cumulus can yield lower turbulence magnitudes.

Mapping where the cloud shadows occur could help determine favorable and unfavorable optical turbulence conditions. Creating maps that model the shadow source, namely the cloud, is the initial step. In Section 6, generating 3-D cloud images from WSI data is described.

6. Stereo Fisheye Cloud Height Estimation

Modern WSI imaging involves a sky-facing camera with a fisheye lens. To deduce cloud heights, a second WSI can be placed a certain distance away (Figure 21). Together, the two images can be analyzed for stereo disparity to estimate the height of the clouds within the field of view as seen in Figure 22. The resultant height map can then be used to generate ground shadows for heat flux computations.

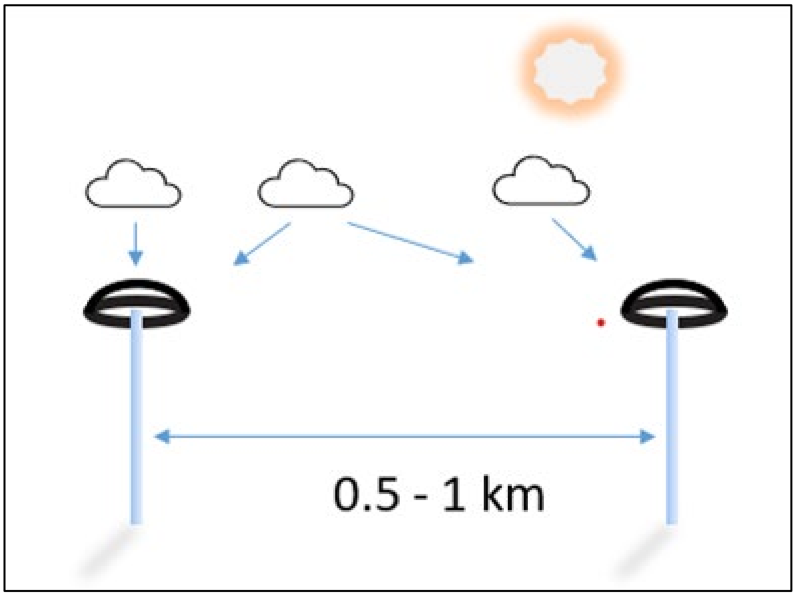

Figure 21. Two WSIs (black hemispheres) mounted on towers separated by ~1 km.

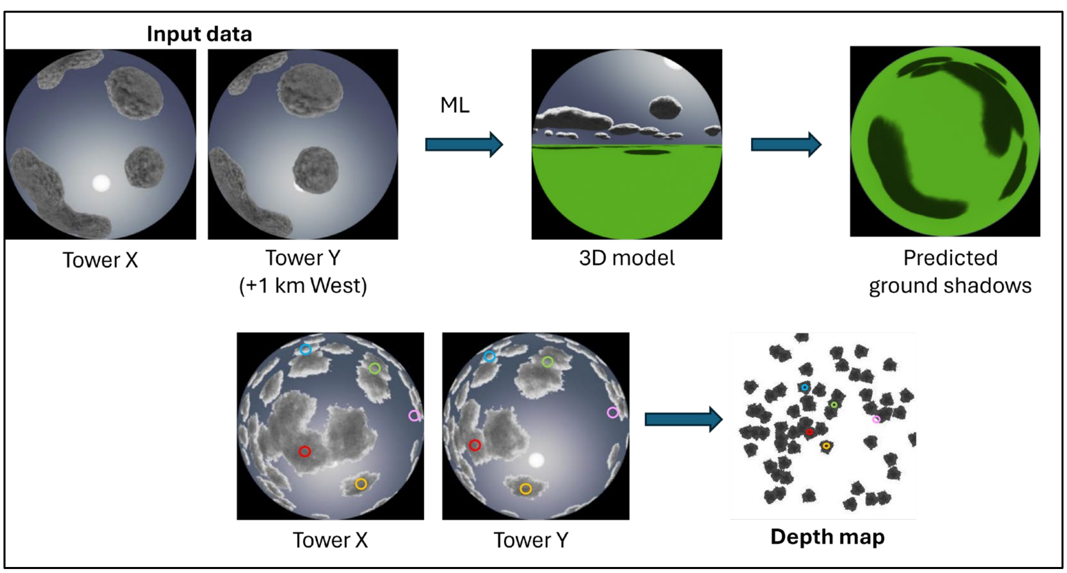

Figure 22. Postprocessing two WSI images into simulating ground shadows.

6.1 Methods

Stereo photogrammetry on fisheye WSI images is a challenge, however, because almost all stereo-disparity algorithms to date use rectilinear imaging (Romps and Öktem 2018; Hamid et al. 2022). The few methods that use fisheye images are geared towards horizontal ground imaging often involving straight edges from artificial objects like buildings and cars (Häne et al. 2014; Schneider et al. 2016). Thus, a new method was developed to deduce cloud positions from paired fisheye cameras.

The principle in solving the stereo fisheye problem is to generate candidates of rectified images proposing the cloud bases exist at a range of different heights. Then, the best height candidate for a region of clouds is the one where the two images have the strongest similarity. This can be formulated within a machine learning model where the two input fisheye images are rectified at a series of candidate heights and then down-sampled via a Siamese convolutional neural network into feature spaces, which are then compared via dot products. The resultant depth map is then generated by a decoding/up-sampling module.

6.2 Results

While the specifics of the machine learning photogrammetry model used here are beyond the scope of this report, some examples of what is possible with synthetic WSI images from the recently published algorithm (Lee et al. 2024) are provided. Cumulus clouds were defined with a 1 km AGL cloud-base height, and cirrus clouds were placed at 10 km AGL.

Figures 23–25 show three diverse examples. For each example, in the bottom-left two images, light gray indicates higher cloud heights (cirrus at ~10 km) and black indicates lower heights (cumulus at ~1 km). In the bottom-right image, black and gray correspond to matching prediction and ground truth, while red and blue correspond to mismatches. In Figure 23 a synthetic pure cumulus cloud example is provided. Here, the model was able to predict the correct placement of cumulus clouds but also inferred some cirrus clouds that were not actually there. In Figure 24, with a mixed cloud deck, the cumulus prediction was adequate, but there was some blurriness and overprediction for the cirrus clouds. Finally, in the cirrus example of Figure 25, the prediction was evaluated as good, though with the same blurriness issue as in Figure 24.

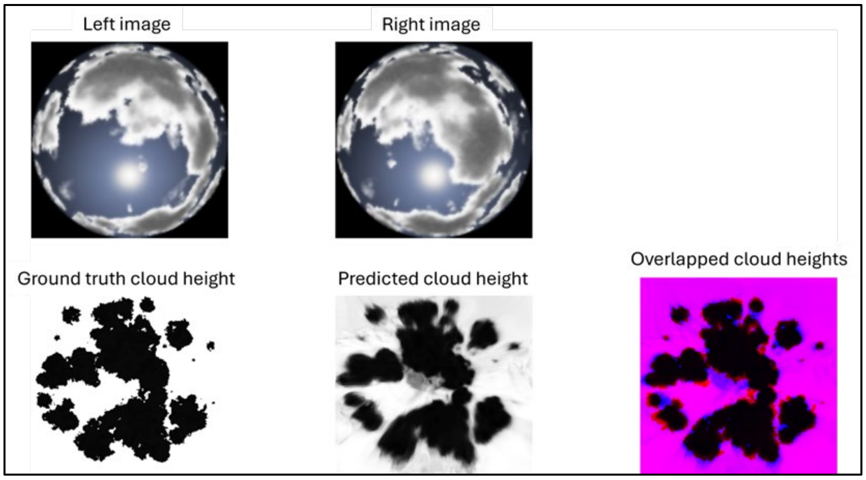

Figure 23. A synthetic pure cumulus cloud example.

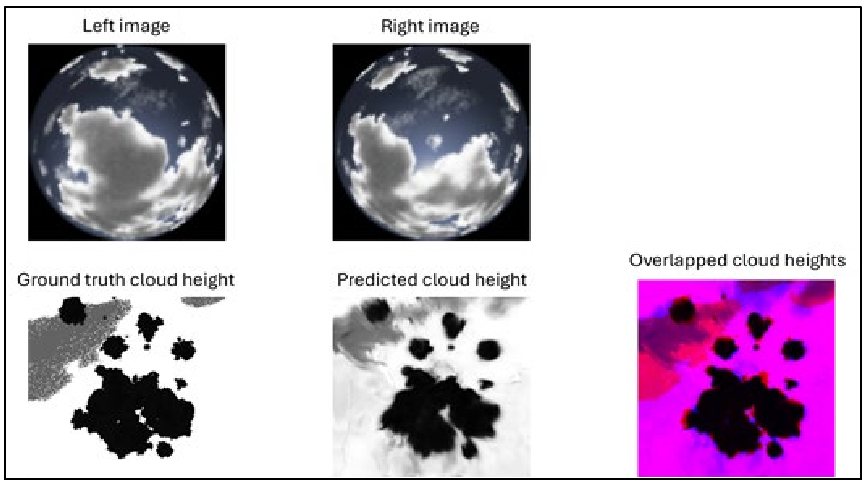

Figure 24. A roughly equal mix of cumulus and cirrus clouds.

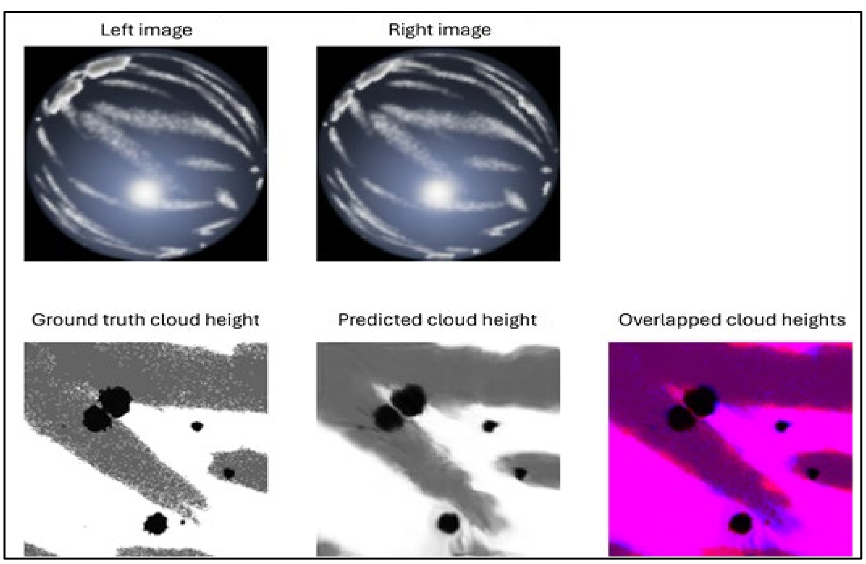

Figure 25. A mostly cirrus plus contrail scenario with a few cumulus examples.

7. Summary and Conclusions

Improved seeing conditions and the propagation of coherent light, such as that of a laser, occur when there are minimal-density variations along the viewed pathway. Unfortunately, the natural state of the atmosphere includes an abundance of density variations. Consequently, when a laser beam traverses the open-air environment, the beam's energy is reduced and/or distorted. The environmental impacts stem from the air's natural chemical composition, resulting in beam absorption and scattering. The air's thermodynamic character produces optical turbulence effects. The index of refraction structure function C_n^2 statistically quantifies the optical turbulence and is largely a function of temperature. Within the atmosphere, vertical temperature gradients are characterized in terms of atmospheric stability. Stability near the Earth's surface is driven by incoming solar radiation. Bringing these variables together under a clear sky, we describe a typical baseline optical turbulence diurnal cycle as follows:

> In short, the clear sky daily cycle begins with incoming solar radiation warming the soil. Once the surface temperatures exceed the air above, an unstable (boiling air) condition develops, creating an optically turbulent environment. This turbulent condition peeks at solar noon after which the waning sun rays create a systematic reduction in the optically turbulent environment. Within an hour of sunset, the lowest layers in the atmosphere become isothermal (neutrally stable), and optical turbulence reaches one of two low points for the diurnal cycle. Overnight the ground perpetually releases warmth that, under a clear sky, results in a stable environment having a modest turbulent status. When the sun rises, the ground is warmed so that a second isothermal (neutral) condition occurs. While this neutrally buoyant condition persists, optical turbulence drops to its second minimum in the diurnal cycle. Such times are also associated with the best long distance seeing conditions.

In addition to the atmospheric composition and thermodynamic properties, the propagation of coherent light is also impacted by cloud shadows.

The most significant cloud shadow impacts begin with a sudden, severe drop in insolation that cascades into a reduction of optical turbulence. Observing from a fixed site, when a cloud passes overhead, the once direct incoming solar radiation can drop by over 50% in less than 10 s, leaving only diffuse energy to warm the same ground. The sharp reduction of surface heat results in cooler air above, inhibiting the vertical mixing (thermal plumes and eddies) of the former actively unstable environment. The lack of convective mechanical turbulence lowers the optical turbulence (C_n^2) within the shadowed area. The condition persists as long as the shadowed environment suppresses the buoyancy/thermal eddies.

Cloud shadow edges are noteworthy in that the sharp temperature differences between the direct (no cloud) and diffuse (cloud) sunlight conditions produce wind shear, leading to increased mechanical turbulence. This transient condition can temporarily increase optical turbulence C_n^2 at the shadow boundary.

Two case studies representing partly cloudy and overcast sky conditions were examined referencing concurrent atmospheric and optical turbulence measurements. Both scenarios had elements of improved optical turbulence. When the area of interest was well within the shadow of a thick cloud, lower C_n^2 was reported. When the cloud cover became an overcast scenario during daylight hours, lower C_n^2 was also observed. When the overcast scenario included a greater release of surface energy than the air could dissipate (late afternoon overcast sky occurring near sunset), this created a turbulent environment due to the warmth being trapped between the surface and the cloud deck overhead (a cloud blanket effect).

Finally, the ability to map cloud shadows was explored by experimentally modeling 3-D clouds. A machine learning–based stereo-photogrammetry model was developed to ingest two WSI images and output the estimated cloud height as a function of rectified ground coordinates.

8. Recommendations

Future work with the sky photogrammetry model will include analyzing actual WSI images from locations separated by more than 1 km to determine cloud heights and arrangement. Meteorological data from the two sites will then be compared against the cloud positions to look for expected and unexpected correlations.

9. References

Amin R, Gould R, Hou W, Arnone R, Lee Z. Optical algorithm for cloud shadow detection over water. IEEE Transactions on Geoscience and Remote Sensing. 2013;51(2).

Hamid MS, Abd Manap NF, Hamzah RA, Kadmin AF. Stereo matching algorithm based on deep learning: a survey. Journal of King Saud University-Computer and Information Sciences. 2022;34(5):1663–1673.

Häne C, Heng L, Lee GH, Sizov A, Pollefeys M. Real-time direct dense matching on fisheye images using plane-sweeping stereo. In: 2014 2nd International Conference on 3D Vision. 2014;1:57–64. IEEE.

Hogan H, Rose M. A history of the laser 1960–2019. Photonics Spectra. 2019 June [accessed 2025 June 30]. https://www.photonics.com/Articles/A_History_of_the_Laser_1960_-_2019/a42279

Lee M, Vaucher G, D'Arcy S, Jane R, Berman M. Whole sky image synthesis for annotated machine learning datasets. Proceedings Volume 13035, Synthetic Data for Artificial Intelligence and Machine Learning: Tools, Techniques, and Applications II; 130350A; SPIE Defense+Commercial Sensing; 2024 June 7; National Harbor, MD. https://doi.org/10.1117/12.3011890

Petty GW. A first course in atmospheric radiation. 2nd ed. Sundog Publishing; 2006.

Pries T. Atmospheric sensitivities of high energy lasers. Air Weather Service Scott Air Force Base (US); 1980 Sep. Report No.: AWS/TN-80/003.

Romps DM, Öktem R. Observing clouds in 4D with multiview stereophotogrammetry. Bulletin of the American Meteorological Society. 2018;99(12):2575–2586.

Schneider J, Stachniss C, Förstner W. On the accuracy of dense fisheye stereo. IEEE Robotics and Automation Letters. 2016;1(1):227–234.

Tatarski VI. Wave propagation in the turbulent medium. Dover Publications, Inc; 1961. p. 285

Vaucher GT, Raby J. Forecasting atmospheric stability transitions over a high-elevation desert in the southwestern United States. J Operational Meteor. 2013;1(9):93–99.

Walters DL, Kunkel KE. Atmospheric modulation transfer function for desert and mountain locations: the atmospheric effects on r0. J Opt Soc Am. 1981;71:397–398.

Appendix A. 2001 Mar 24: General Meteorological Conditions

Figure A-1 shows meteorological measurements over a high elevation location in a southwestern U.S. desert, which coincides with the 2001 Mar 24 case study. This dataset was selected for its demonstration of a clear morning, partly cloudy midday, and its relatively clear afternoon.

All data displayed are within the same 1-km pathway. C_n^2 is sampled along reciprocal paths (0 →1 km; 1→ 0 km). Solar radiation is sampled at Site B (the 1-km location) at 2 m above ground level (AGL). Temperatures and their 16-m minus 2-m gradient are sampled mid-path at a 500-m site. Wind speed and wind direction are sampled at Site B (the 1-km site) at 8 m AGL.

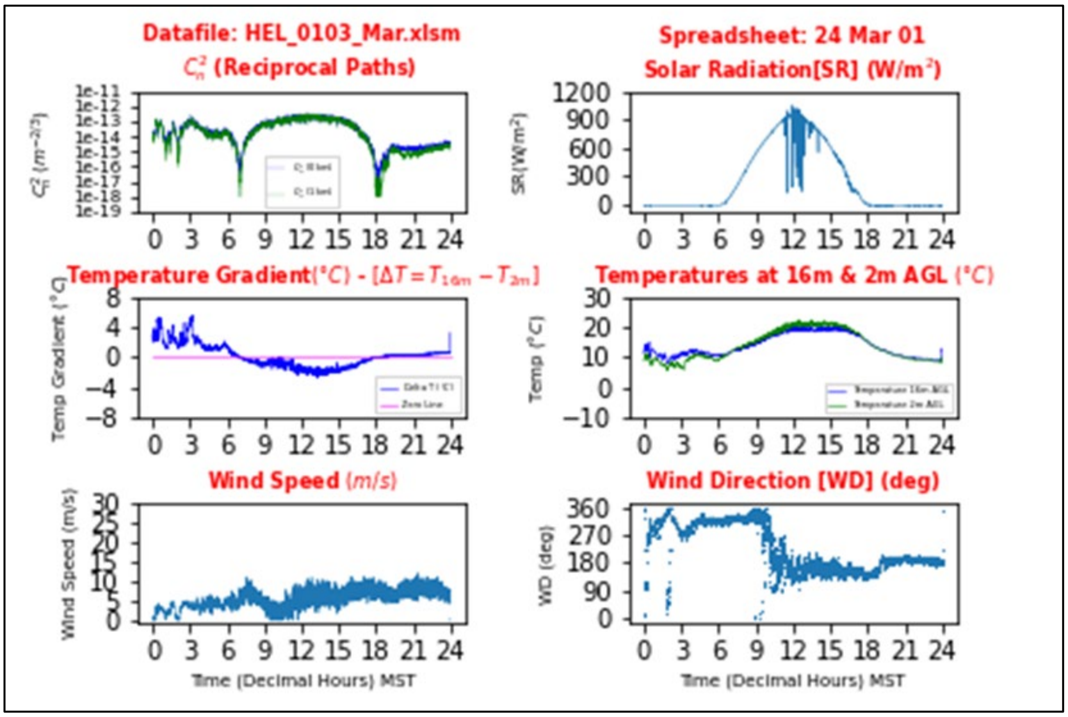

Figure A-1. 2001 Mar 24 meteorological data time series.

Appendix B. 2001 June 7: General Meteorological Conditions

Figure B-1 shows meteorological measurements over a high elevation location in a southwestern U.S. desert, which coincides with the 2001 June 07 case study. This dataset was selected for its demonstration of partly cloudy and overcast conditions. Partly cloudy conditions occur in the mid-morning through early afternoon, followed by overcast sky from mid-afternoon through evening.

All data displayed are within the same 1-km pathway. C_n^2 is sampled along reciprocal paths (0 →1 km; 1→ 0 km). Solar radiation is sampled at Site B (the 1-km location) at 2 m AGL. Temperatures and their 16-m minus 2-m gradient are sampled mid-path at a 500-m site. Wind speed and wind direction are sampled at Site B (the 1-km site) at 8 m AGL.

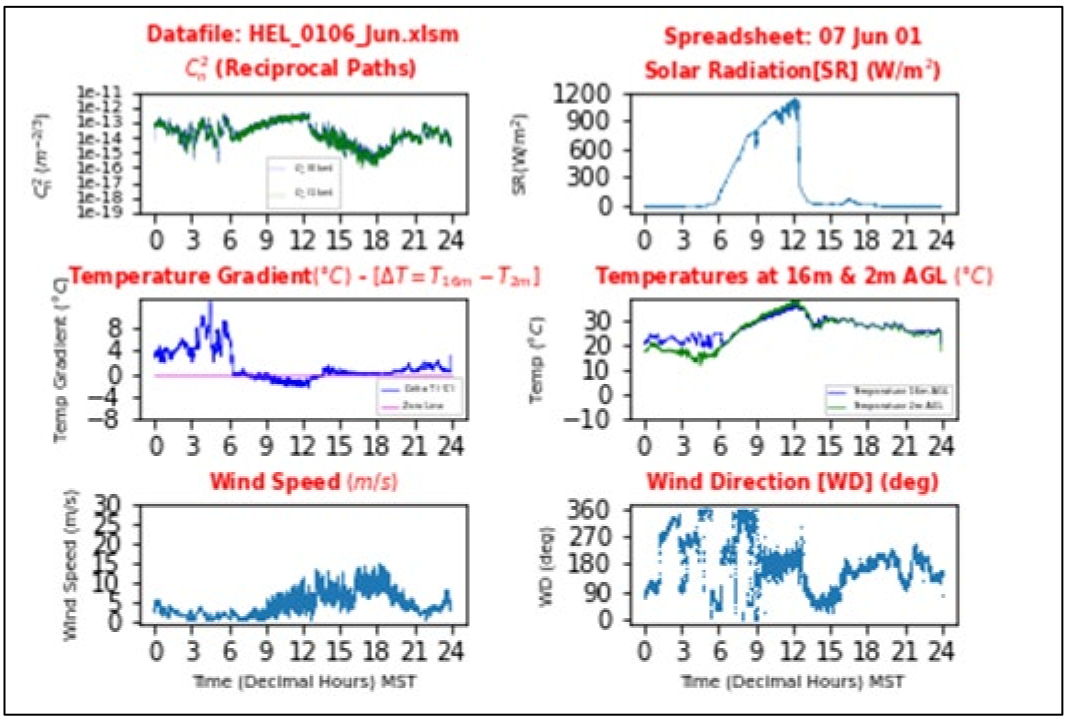

Figure B-1. 2001 June 07 meteorological data time series.

List of Symbols, Abbreviations, and Acronyms

3-/4-D	Three-/Four-Dimensional
AGL	Above Ground Level
CH_4	Methane
C_n^2	Index of Refraction Structure Function
CO_2	Carbon Dioxide
ΔT	Delta Temperature ($T_{final} - T_{initial}$)
DE	Directed Energy
H_2O	Water
HEL	high energy laser
LASER	Light Amplification by Stimulated Emission of Radiation
MST	Mountain Standard Time
n	Index of Refraction
N_2O	Nitrous Oxide
O_3	Ozone
P	Pressure
T	Temperature
WSI	Whole Sky Imager

1 (PDF)	DEFENSE TECHNICAL INFORMATION CTR DTIC OCA
1 (PDF)	DEVCOM ARL FCDD RLB CI TECH LIB